

Structure and Response to Flow of the Glycocalyx Layer

Eduardo R. Cruz-Chu,[†] Alexander Malafeev,[‡] Tautrimas Pajarskas,[†] Igor V. Pivkin,[‡] and Petros Koumoutsakos^{†‡*}

[†]Computational Science and Engineering Laboratory, ETH, Zurich, Switzerland; and [‡]Scientific Computing Group, Institute of Computational Science, University of Lugano, Lugano, Switzerland

ABSTRACT The glycocalyx is a sugar-rich layer located at the luminal part of the endothelial cells. It is involved in key metabolic processes and its malfunction is related to several diseases. To understand the function of the glycocalyx, a molecular level characterization is necessary. In this article, we present large-scale molecular-dynamics simulations that provide a comprehensive description of the structure and dynamics of the glycocalyx. We introduce the most detailed, to-date, all-atom glycocalyx model, composed of lipid bilayer, proteoglycan dimers, and heparan sulfate chains with realistic sequences. Our results reveal the folding of proteoglycan ectodomain and the extended conformation of heparan sulfate chains. Furthermore, we study the glycocalyx response under shear flow and its role as a flypaper for binding fibroblast growth factors (FGFs), which are involved in diverse functions related to cellular differentiation, including angiogenesis, morphogenesis, and wound healing. The simulations show that the glycocalyx increases the effective concentration of FGFs, leading to FGF oligomerization, and acts as a lever to transfer mechanical stimulus into the cytoplasmic side of endothelial cells.

INTRODUCTION

The functioning of the human metabolism requires transfer of nutrients, gas molecules, and hormones from the bloodstream into the target organs. Such exchange between circulating blood and the tissues occurs across a thin layer of endothelial cells located in the luminal surface of the blood vessels, known as the endothelium. The endothelium forms the inner cellular lining covering the entire vascular network, from the wide heart arteries to the smallest capillaries (1). Far from being an inert tissue, the endothelium is very versatile, and it is conveniently heterogeneous (2), adapting itself to the local environment. Moreover, the endothelium participates actively in critical biological processes such as blood cell trafficking, angiogenesis, and immune response (3), and its malfunction is related to several diseases (4,5).

The glycocalyx is the outermost part of the endothelium. Located at the surface of endothelial cells, the glycocalyx is the first vascular barrier in direct contact with blood. Fig. 1 shows an atomic model of the glycocalyx in the context of the circulatory system. As its name states, the glycocalyx is a sugar-rich layer, with carbohydrates associated by covalent links forming oligosaccharide chains that can be either long and linear or short and branched. The presence of anionic oligosaccharides, such as heparan sulfate, provides the glycocalyx layer with a characteristic negative charge. Most oligosaccharides are covalently attached to membrane proteins, but it is also possible to find that some are free and remain adsorbed in the glycocalyx region by noncovalent interactions. Furthermore, the glycocalyx can retain plasma proteins recruited from extracellular space and its thickness can be lessened by enzymatic and shear-induced shedding,

producing a dynamic equilibrium between its composition and the flowing blood (6). Due to the variety of its composition and its exposed location, the glycocalyx plays two critical functions for the endothelium: as an interface between chemical signals in the blood and biochemical pathways inside cells; and as a barrier against chemical or mechanical damage.

In early studies of the endothelium, the glycocalyx had remained unnoticed because it was difficult to visualize: the tiny sugar coat was washed out by the preparation procedures involved in conventional light and electron microscopy. The first visual evidences of the glycocalyx came through the employment of cationic dyes, such as ruthenium red, which were strongly adsorbed by the negatively charged glycocalyx (7). Further improvements in staining protocols as well as in spectroscopic methods have allowed obtaining static images of the glycocalyx (1). Since then, research in glycocalyx has flourished and now it is investigated as a therapeutic target against several pathologies, such as atherosclerosis (8) and diabetes (9). Furthermore, recent experimental studies hypothesize a long-range effect of glycocalyx on water ordering (10), which may mediate cell surface interactions.

Due to the experimental difficulty of tracing the elusive atomic events inside the glycocalyx, researchers have turned to computer simulations (11–16). Those models were mostly based on continuum or coarse-grained approaches but refined to include the peculiarities of the glycocalyx, such as the negatively charged surface or the steric resistance of oligosaccharide chains. Although computer simulations have contributed to contemporary understanding of the glycocalyx, structural information is still much needed to advance the field. We turn to all-atom molecular dynamics (MD) simulations, which provide the most detailed and dynamic representation of biomolecular systems (17,18).

Submitted April 21, 2013, and accepted for publication September 30, 2013.

*Correspondence: petros@ethz.ch

Editor: Nathan Baker.

© 2014 by the Biophysical Society
0006-3495/14/01/0232/12 \$2.00

<http://dx.doi.org/10.1016/j.bpj.2013.09.060>



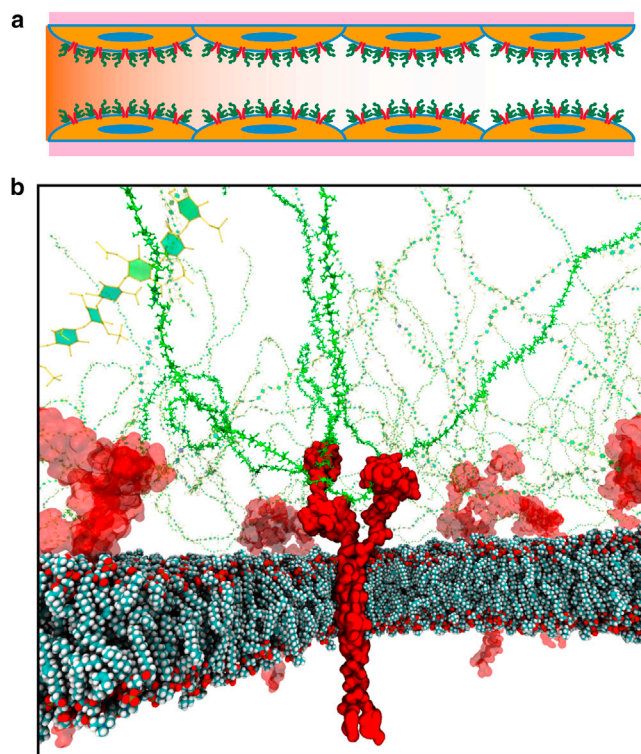


FIGURE 1 Glycocalyx in the circulatory system. (a) A cartoon representation of a blood vessel: (orange circles) endothelial cells; (green brush) glycocalyx. (b) All-atom model of the glycocalyx. (Green licorice representation) Sugar chains. (Red surfaces) Transmembrane protein; (van der Waals beads) lipid bilayer. Water and ions are not shown.

Here, we report large-scale, all-atom MD simulations of the glycocalyx layer. To begin, we describe a procedure to build all-atom models of glycocalyx. We present structural insight obtained while building the model: the folding of the ectodomain of proteoglycans, the extended conformation of sugar chains, and the negligible effect of sulfonation charge on the chain length. Finally, our model was simulated under nonequilibrium conditions to address two fundamental questions about the glycocalyx: its response to mechanical stimuli under shear flow, and its ability to retain fibroblast growth factor (FGF) proteins.

METHODS

MD simulations compute the time-evolution of a many-body system by solving Newton's equations of motion. Two compulsory requirements for MD simulations are the initial atomic positions of particles, and the force field describing the interactions between particles. The glycocalyx is intrinsically disordered and it is not possible to obtain a minute atomic structure by NMR or crystallography; thus, the atomic models relevant to this discussion were built based on the available structural information as detailed below.

The MD simulations are organized into three groups:

The first group involves simulations (Sim) needed to build the glycocalyx structure (Sim1–32 in Table 1): i.e., annealing of ectodomain (Sim1–24), equilibration of transmembrane (Sim25–26) and cytoplasmic (Sim27–28) domains, and the assembly of 5,700,000-atom glycocalyx systems (Sim29–32).

The second group relates to glycocalyx simulations under shear flow (Sim33–35).

The third group lists simulations used to study binding of proteins to the glycocalyx (Sim36–40).

Building the glycocalyx

We chose Syndecan-4 (Syn-4) proteoglycan and heparan sulfate (HS) sugar chains for modeling the glycocalyx as described in the Results and Discussion. Below we provide information about assembly protocol, simulation time, and system size.

We initially divided the glycocalyx structure into three parts: Syndecan-4 ectodomain (Syn-4 Ect) linked with sugar chains; Syndecan-4 transmembrane (Syn-4 Tmb) dimer embedded into a lipid bilayer; and Syndecan-4 cytoplasmic (Syn-4 Cyt) dimer. Fig. S1 in the Supporting Material shows the three separate systems. After reaching equilibration for each part, the sections were glued together into a single glycocalyx system and equilibrated further.

For Syn-4 Ect simulations (Sim1–24), our starting structure was a fully stretched ectodomain joined with three extended 100-residue sugar chains. Subsequently, the structure was annealed as follows: the system was heated at 1000 K for 10 ns, then cooled down to 310 K at a rate of -100 K/1 ns. After that, the structure was checked for stereochemical correctness (19). The final annealing stage was an equilibration of 100 ns, summing a total of 116 ns per annealing cycle. The tested range of temperatures does not allow employing all-atom water models; therefore, an implicit solvent model was used. We simulated four different HS sequences (see Fig. 2 and the Results and Discussion). Six different conformations were tested for each HS sequence. The chains orientations were random, but avoided overlapping contacts between residues. All together, the simulation time spent in annealing cycles was

$$(4 \text{ HS options}) \times (6 \text{ conformations}) \\ \times (116 \text{ ns per cycle}) = 2.784 \mu\text{s}.$$

For Syn-4 Tmb simulations, we mapped two Syn-4 backbones into a reported Glycophorin-A dimer structure (20) (PDB:1AFO; see Results and Discussion). Weinbaum et al. (15) have proposed a hexagonal symmetry for glycocalyx. In accordance with such model, Syn-4 transmembrane dimers were embedded into a POPC lipid bilayer of hexagonal periodicity and 820 nm^2 area. The lipid membranes were generated from a preequilibrated membrane patch provided with the MEMBRANE BUILDER plugin available in the software package VMD (21). Two systems were built, the first containing one Syn-Tmb dimer, the second with three Syn-Tmb dimers equally spaced among themselves and their periodic images. Then, the systems were covered with water boxes resulting in 11-nm height each. Both systems were equilibrated in NPT ensemble for 5 ns (Sim25–26).

For Syn-4 Cyt simulations, we solvated and ionized a Syn-4 cytoplasmic dimer (22) (PDB:1EJP) using a water box of $8 \times 8 \times 9 \text{ nm}^3$. Then, the system was equilibrated for 5 ns in NPT ensemble (Sim27), followed by 5 ns in NVT (Sim28).

The final stage is to join all three parts: the transmembrane domain contains residues 141–171; the ecto domain, 1–141; and the cytoplasmic domain, 171–198 (see Fig. 2). The repeating residues in the transmembrane part were used as guiding positions to attach the other domains. Special care was taken to avoid sugar rings either intersecting each other across the periodic images or overlapping the membrane region. Once the three parts were joined, topology was reconstructed around the new bonds and the entire structure was checked for chirality correctness. Two systems were built, with one and three Syn-4 dimers, then solvated and ionized to 100 mM NaCl concentration. The final systems are composed of 5,700,000 atoms, with 820 nm^2 area and 69 nm height. MD equilibrations proceeded as follows: 3.5 ns in NPT ensemble (Sim29–30) and 5 ns in NVT (Sim31–32). The final equilibrated structures for both glycocalyx systems are provided in the Supporting Material.

into a three-dimensional grid. Overall, the protocol for binding simulations is similar to the molecular-dynamics flexible fitting technique (24), where biomolecules are force-fitted into cryo-electron microscopy grids. In our case, the flowing proteins are force-driven into glycocalyx grids. The grids were calculated using the PMEPOT (25) plugin available with the software VMD. PMEPOT calculates the electrostatic potential from a MD trajectory by recomputing the long-range electrostatic forces via particle-mesh Ewald (PME) (26). Two grids were computed, one for the system with one Syn-4 dimer, the other for the system with three Syn-4 dimers. We characterized the glycocalyx grids by the average electrostatic potential of 5-ns MD equilibration trajectories (Sim31 and 32), using only the atomic charges of HS chains, whereas other components, such as Syn-4 dimers, lipid membrane, and electrolytic solution were not included. This simplification was necessary to provide a smooth potential that drives flowing proteins near highly charged sugar locations within dozens of nanoseconds. In the [Supporting Material](#), we include references to a Grid-SMD tutorial and the glycocalyx grids.

The flowing protein is fibroblast growth factor-2 (FGF-2) (PDB:1BFB). We refer to the Results and Discussion for more details about FGF-2. To induce flow, a force of 1 pN was applied to the α -carbons of FGF-2, with the direction of the force being along the x axis. For binding simulations, we performed a three-step MD cycle.

For the first part (Sim36), 10 all-atom FGF-2 proteins were randomly distributed on a region from 14 to 39 nm above the membrane location. The minimum distance between FGF-2's centers of mass was 5 nm. Periodic boundary conditions were assumed, and the periodic lengths matched the glycocalyx grid dimensions. Then, FGF-2 molecules were allowed to flow for 10 ns.

For the second part, two separate 10-ns MD simulations were performed, one with the single Syn-4 dimer glycocalyx grid (Sim37) and the other with the three Syn-4 dimer glycocalyx grid (Sim38). The starting point was the last frame of Sim36, but now the glycocalyx grids were active, affecting FGF-2 flow dynamics.

For the third part, both Sim37 and 38 simulations were continued for 10 ns, but the glycocalyx grids were turned off (Sim39 and 40, respectively). For all three parts, implicit solvent was used. To maintain FGF-2 structure, secondary structure restraints were used and the steering forces derived from the grid were scaled up by a factor of 0.05. The system size was 20,180 atoms, consisting of only 10 FGF-2 molecules.

Protocol details

All MD simulations were performed using the software program NAMD 2.7 (27). We used the CHARMM biomolecular force field (28) and the TIP3P water model (29). Structures were generated using the PSFgen utility provided with the VMD program. The latest additions to CHARMM include parameters for sugars (30–32). To assure compatibility with PSFgen, atom types were renamed from the six-letter code given in the CHARMM force field into a four-letter code. Sulfamate group parameters (R-NHSO_3^-) needed for sulfonated GlcNAc were taken from Huige and Altona (33).

For MD simulations with implicit solvent, namely annealing (Sim1–24) and binding (Sim36–37) simulations, we used 1-fs timestep and flexible bonds. We employed the generalized Born implicit solvent (34) that accurately represents the dielectric screening between solute molecules in electrolytic solution. The van der Waals and electrostatic interactions were calculated using a cutoff of 16 Å with a switching function starting at 15 Å and 0.1 M electrostatic screening. Temperature was controlled using a Langevin thermostat. For MD simulations with explicit water (Sim25–35), we used a 2-fs timestep, rigid bonds, and PME electrostatics with a grid density of $1/\text{\AA}^3$. The van der Waals interactions were calculated using a cutoff of 12 Å with a switching function starting at 10 Å. Simulations in NPT ensemble were kept at 1 atm pressure and 310 K using a Langevin thermostat and a Nosé-Hoover Langevin piston. Simulations in the NVT ensemble were kept at 310 K using the Andersen thermostat. To simulate

6,000,000 atom systems, we used the memory-optimized version of NAMD (35).

The analysis was performed using VMD (Visual Molecular Dynamics, University of Illinois at Urbana-Champaign, Champaign, IL), MATLAB (The MathWorks, Natick, MA), and PYTHON (Python Software Foundation, Wilmington, DE) scripts. All MD snapshots were made with VMD. The secondary structure plots (Fig. 3 *a*), were computed using the TimeLine plugin in VMD. To calculate the velocity profiles, the system was divided in layers of 1 nm height along the z axis; for each layer, the velocities in the x axis of water oxygens were averaged. The shear stresses (τ) were computed from the resulting velocity profiles as

$$\tau = \mu \frac{\delta v}{\delta z},$$

where μ is the viscosity of the TIP3P water model (36) ($0.321 \text{ mPa} \cdot \text{s}$); and $\delta v / \delta z$ is the gradient of the x velocity along the z axis. The persistence length (P_C) was calculated using the relationship

$$\langle e^2 \rangle = 2P_C L_C - 2P_C^2 [1 - \exp(-L_C/P_C)],$$

where $\langle e^2 \rangle$ is the averaged squared end-to-end distance, L_C is the contour length, and P_C is the persistence length (37).

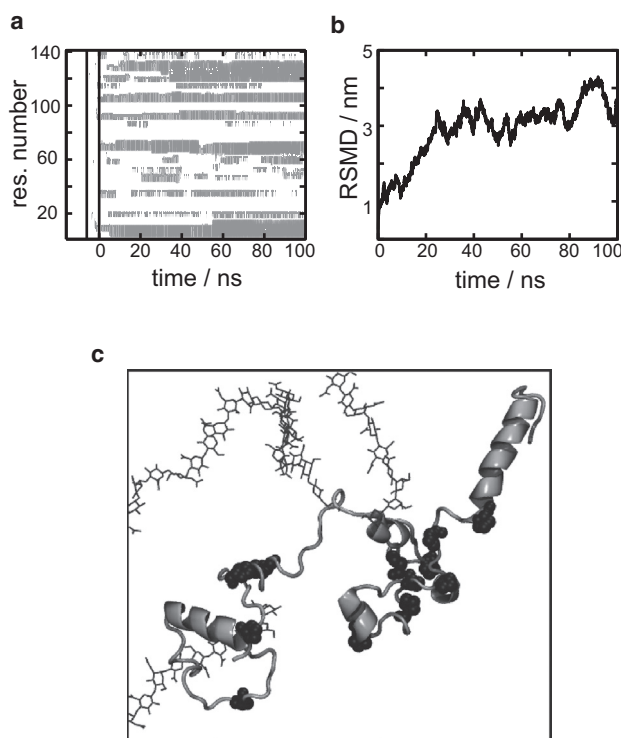


FIGURE 3 Ectodomain folding. (*a*) Plot shows the time evolution of secondary structure for Syn-4 ectodomain during the annealing cycle. Abscissa and ordinate axes show time and residue number, respectively. (*Vertical lines*) The three annealing stages: 10 ns heating at 1000 K, 6 ns cooling from 1000 to 310 K, and final 100-ns equilibration at 310 K. (*Shaded bands*) Appearance of α -helical structure. (*b*) RMSD of α -carbons of Syn-4 during equilibration at 310 K. (*c*) (*Snapshot*) Last frame of simulation, with (*shaded ribbons*) α -helices, (*solid spheres*) proline residues, and (*lines*) HS chains.

RESULTS AND DISCUSSION

Building glycocalyx system

The glycocalyx layer is composed of sugar chains covalently linked to transmembrane proteins located at the surface of endothelial cells. A complete all-atom model of the glycocalyx is notoriously difficult to build: the oligosaccharide chains are very heterogeneous in structure and sequence to be resolved by crystallization or NMR and only low-resolution images are available (38–40). To overcome this problem, most glycocalyx models have only considered some key features such as negative charge or polymer hindrance (11–16), while disregarding other equally important features such as nonuniform charge distribution, realistic sugar chain length, or interactions among the different biomolecular components.

We aimed to build the most detailed all-atom glycocalyx model using structural information. Some degree of simplification is required for a system with such high structural heterogeneity, but we did preserve the molecular components that are most prevalent in glycocalyx. The most abundant oligosaccharides in the glycocalyx are heparan sulfate (50–90%) and chondroitin sulfate (10–20%) (6). Accordingly, our glycocalyx considers heparan sulfate (HS) chains. The anchoring transmembrane proteins for HS chains are syndecans. We chose Syndecan-4 (Syn-4), which is widely distributed among all endothelial cells, in contrast to other syndecans that are localized in specific tissues (41). Syn-4 is a proteoglycan of 198-amino-acid length, containing extracellular, transmembrane, and cytoplasmic domains. The extracellular domain (i.e., the ectodomain) contains three points for attaching HS molecules (42). Fig. 2 presents the employed Syn-4 and HS sequences.

Based on data from electron microscopy images (38), Weinbaum et al. (15) have presented a quasiperiodic hexagonal arrangement for a glycocalyx with a spacing of 100 nm between proteoglycan clusters. Also, HS chains are long linear polymers of ~100–200 sugar residues, corresponding to 50–100-nm length (1,43). An all-atom model with such spacing and dimensions would demand ~100,000,000 atoms, which is at the limit of contemporary MD capabilities. To reduce the computational cost of building the structure, the system was initially split into three smaller pieces: Syn-4 ectodomain linked with HS chains; Syn-4 transmembrane dimer embedded into a lipid bilayer; and Syn-4 cytoplasmic dimer (see Methods).

The first topology block is Syn-4 ectodomain joined with three HS chains. The HS length is assumed to be 100 sugar residues (44). The HS chains are covalently attached to three serine residues at positions 39, 61, and 63 in the ectodomain. The linker between HS and ectodomain has been described in other publications (6,45). In short, HS and Syn-4 are joined through a tetrasaccharide GlcA- $[\beta 1-3]$ -Gal- $[\beta 1-3]$ -Gal- $[\beta 1-4]$ -Xyl (see Fig. 2). At the reducing end (*right-hand side* of Fig. 2, *b–e*), a xylose sugar attaches to a serine

amino acid through $\beta 1$ glycosidic linkage. The HS chain grows at the nonreducing end (*left-hand side* of Fig. 2, *b–e*) by adding either GlcA- $[\beta 1-4]$ -Glc- $[\alpha 1-4]$ or IdoA- $[\alpha 1-4]$ -GlcNAc- $[\alpha 1-4]$ disaccharide units. The former disaccharide appears in nonsulfonated form, also known as the NA region. The latter disaccharide can be either partially sulfonated (NA/NS region) or highly sulfonated (NS region). A HS chain usually contains alternating NA, NA/NS, and NS regions of variable length, and the specific sequence seems to correlate with the cell type origin (45). Although increasing evidence suggests precise sulfonation patterns with strong specificity for particular proteins (46), current experimental techniques can only partially resolve HS sequences (47). To provide the closest model to a real glycocalyx, the sulfonation patterns for NS and NA/NS regions were chosen to bind fibroblast growth factor and antithrombin, respectively (45) (see Fig. 2 *b*). At the non-reducing end, we adopted the sulfonation pattern proposed by Wu and Lech (48).

Due to the presence of 12 proline residues and a lack of homology structures, the ectodomain is usually depicted in a centipedelike representation; that is, as an elongated protein stretching away from the cellular membrane with HS chains branching out from the unfolded protein backbone (1,41,44,49,50). Because MD simulations have been remarkably successful in the study of folding processes for proteins of similar size (51), we decided to test the ectodomain structure using a simulated MD annealing procedure (see Methods). We took advantage of the small system size, ~9000 atoms, to simulate four HS sequences. For each HS sequence, six simulations were performed, using different initial conformations. The sequence employed were: a combination of NA-NA/NS-NS domains (Fig. 2 *b*, Sim1–6); a nonsulfonated NA domain (Fig. 2 *c*, Sim7–12); a fully sulfonated NS domain (Fig. 2 *d*, Sim13–18); and a chimeric protonated domain, called NAH (Fig. 2 *e*, Sim19–24).

Fig. 3 shows the ectodomain folding for one annealing cycle with NA-NA/NS-NS sugar chains. Similar plots were observed for all systems and the use of NA, NS, and NAH sequences did not lead to any significant difference in folding. Fig. 3 *a* reveals the appearance of secondary structure in the ectodomain. There is no protein structure during the heating stage, but as the system is cooled down and progresses in the 310 K equilibration stage, α -helices form at both ends of the ectodomain.

It is worth noting that the linker positions remain unfolded and accessible. Moreover, the structure is still highly flexible. Fig. 3 *b* shows the RMSD calculated from α -carbons during the equilibration stage. After 40 ns of initial folding, the RMSD oscillates within a wide region of 1.5 nm, lacking the plateau characteristic of stable folded structures. Our results propose a very mobile ectodomain with a combination of folded conformation at both ends and unfolded coils at the center, where HS molecules are

linked. Fig. 3 *c* shows a snapshot of the final frame of annealing. Conversely, there was no appearance of compact structure for the HS chains, and they remain unfolded for all sequence options.

Fig. 4 shows the average end-to-end distance for HS chains during the 310 K equilibration stage. Remarkably, such distance is approximately the same for different HS sequences—insensitive to the total charge and sulfonation pattern. The lack of correlation between sequence and end-to-end distance in our annealing simulations is attributed to three causes:

1. The HS chains are hydrophilic; therefore, they favor the extended conformation in solution.
2. There is a limitation of the solvent model, the generalized Born implicit solvent, which does not compute long-range electrostatic forces. Such long-range interaction should affect the conformation of a highly charged polymer.
3. There is a lack-of-crowding effect, in which each annealing simulation contains only three HS chains. A higher HS concentration should force the HS chains to stretch due to electrostatic repulsion and steric clashes.

A quantity of interest is the bending stiffness (EI), which is widely used in mesoscopic models of glycocalyx (43,52). We estimated the EI of HS chains using the final stage of the annealing cycle, namely the equilibrations at 310 K for 100 ns. To represent stiffness, we first calculated the persistence length (P_C). The procedure to compute P_C is described in the Methods. Then, we employed

$$P_C = \frac{EI}{k_B T}, \quad (1)$$

where k_B is the Boltzmann constant, and T is 310 K.

P_C was calculated for all four sulfonation patterns. A table listing P_C and EI values is included in the Supporting

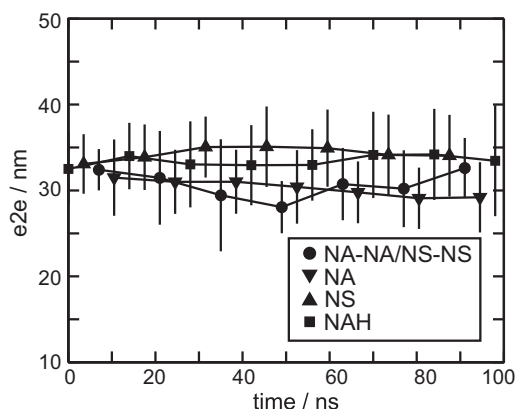


FIGURE 4 Effect of sulfonation pattern on the conformation of HS chains. The plot shows end-to-end distance for all HS sequence alternatives. Each point represents an average taken over 18 HS chains. Error bars represent \pm SD taken over 18 HS chains. Overlapping regions in the error bars highlight the variability in the end-to-end distance values.

Material. Similar to the end-to-end distances, the P_C for HS chains was not sequence-dependent. Also, the P_C values were highly variable, with a mean value of 15.92 nm, in good agreement with previously reported P_C values for all-atom sugar models (37).

The EI mean value for HS chains is 68.28 pN nm², approximately an order-of-magnitude lower than 490 pN nm², the value commonly used in continuum models. Note that to obtain an EI of 490 pN nm², the P_C value should be 114.5 nm, which is unrealistic for HS chains. We conclude that the high EI value for glycocalyx cannot be attributed to the HS chains alone. The other macromolecular components of the glycocalyx, such as plasma proteins and adsorbed carbohydrate chains, contribute to an enhanced stiffness. Although our glycocalyx models include atomic information, they still lack the heterogeneity added by the adsorbed molecules.

The second topology block is the transmembrane domain. As yet, there is no high-resolution structure available; nevertheless, there is cumulative experimental evidence that all syndecans have α -helical transmembrane domains and appear as dimers (53,54). In a recent computational study, Psachoulia et al. (55) have shown that Syn-2 and Glycophorin-A share the same transmembrane dimer packing, where both α -helices are in contact through a GXXXG sequence motif. Because Syn-2 and Syn-4 transmembrane domains share 78% amino-acid identity and the GXXXG motif (residues 153–157, see Fig. 2 *a*), we overlapped two Syn-4 backbones into a reported Glycophorin-A dimer structure. Dimer transmembrane domains were inserted into a POPC lipid bilayer. Two systems were built, the first with one dimer, the second with three dimers, then inserted into a lipid bilayer and equilibrated as described in Table 1.

The last topology block, namely the cytoplasmic domain, is well characterized experimentally and high-resolution dimeric structures are available. During equilibration, the structure remained as a dimer, but both ends showed high mobility. Certainly, we hypothesize that attachments to the transmembrane domain at N-terminus and to actin filaments at the C-terminus are necessary to restraint mobility.

The final stage is to join all three parts into a single glycocalyx system, then solvate and ionize it, resulting in a system of 5,700,000 atoms. The entire glycocalyx system was equilibrated further (Sim29–32). Equilibrium states were checked by convergence of temperature, volume, pressure, and total energy. A snapshot of the final frame for the three Syn-4 dimer systems with periodic images is presented in Fig. 1 *c*. Movie S1 in the Supporting Material shows the NVT equilibration of the three-dimer system.

Shear-stress effect on glycocalyx conformation

The endothelial cells are responsive to mechanical stimuli from the flowing blood (56), controlling vessel diameter (57), vessel permeability (58), and flux of biochemical

signals (59,60). The glycocalyx is in direct contact with the bloodstream and mediates these stimuli by transmitting the flow-induced shear stress and pressure into the interior of endothelial cells. In turn, the glycocalyx conformation also affects the migration of blood cells and plasma proteins through the vasculature.

We study the effects of shear flow using one of our glycocalyx structures, namely the system with three Syn-4 dimers and 18 HS chains (Fig. 1 c), which has the highest glycocalyx concentration. To induce shear stress, we apply forces on the solvent located in the ectoplasmic side. We performed three simulations in the NVT ensemble, using forces of 0.1 pN (Sim33), 0.01 pN (Sim34), and 0.001 pN (Sim35). Such forces result in applied shear stress values of 30.42, 3.63, and 0.47 MPa, respectively.

The flow simulations with shear stress of 30.42 and 3.63 MPa damage the integrity of glycocalyx, as the Syn-4 ectodomains unfold. Fig. S2 shows the final frames of those simulations. For flow simulation under shear stress of 0.47 MPa, Syn-4 ectodomains maintain their structures and only the HS chains are straightened by the flow. Fig. 5 shows the initial and final frame as well as the velocity and shear stress profiles. The velocity profile is largely parabolic above the glycocalyx, but it becomes approximately linear inside the sugar layer. Accordingly, the highest shear stress is observed at the top border of glycocalyx and it decreases close to the membrane.

We further analyzed this simulation by computing the HS charge density and the cytoplasmic domain conformation. Fig. 6 a presents the time-evolution of HS charge density.

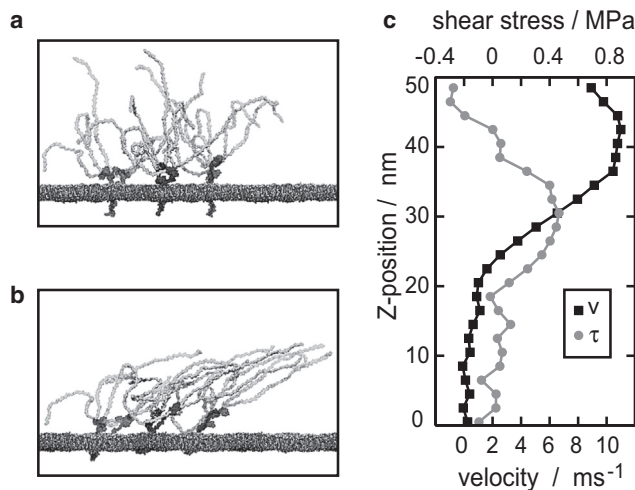


FIGURE 5 Effect of shear flow on glycocalyx conformation. (a) Initial conformation of the system: a glycocalyx layer composed of three Syn-4 dimers (solid) embedded into a lipid bilayer (dark shaded) and 18 HS chains (light shaded). The flow is applied on the upper half of the ectoplasmic compartment (see text). A graphene barrier was located at 51 nm above the lipid membrane (not shown here). (b) Bending of glycocalyx under 0.47 MPa shear stress. (Snapshot) Simulation after 10 ns, periodic images of the lipid membrane are shown repeated along the x axis. (c) Velocity (solid squares) and shear stress profiles (shaded circles).

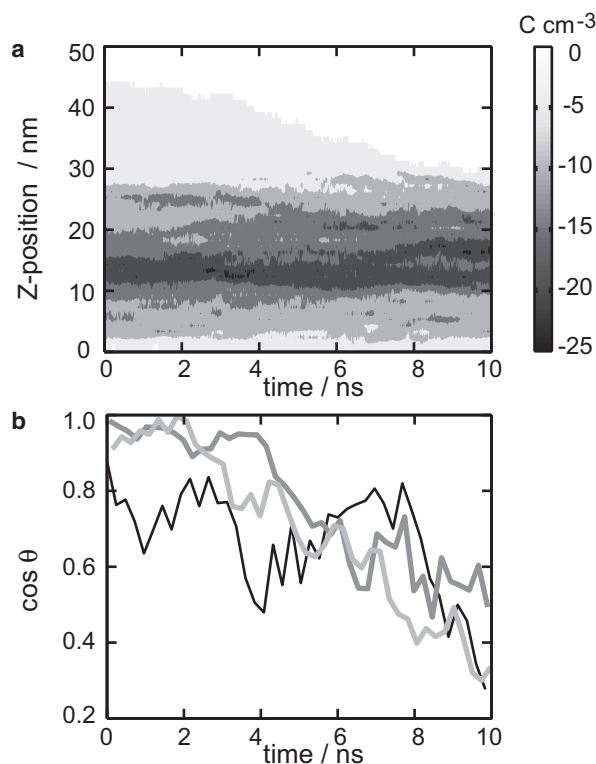


FIGURE 6 Conformational change of glycocalyx for 0.47 MPa shear stress flow simulation. (a) The contour plot shows the charge density of HS chains in the ectoplasmic compartment. The abscissa represents time; the ordinate represents position above the lipid membrane. The values of the charge density are color-coded according to the color-bar at the right. (b) The plot shows the variation of angle for the three cytoplasmic domains of Syn-4 dimers; each line represents one dimer.

Initially, the charge density occupies a region up to 45 nm above the lipid membrane. As the flow impacts the HS chains, the glycocalyx conformation changes, crowding the HS chains into a smaller volume. The charge distribution changes accordingly, compressing the negative charges into a region of 30 nm within the membrane. Although the flow changes the distribution of charges from 45 to 30 nm above the membrane, the highest charge concentration remains located in a region between 10 and 15 nm above the membrane during the entire simulation (see Fig. 6 a). Furthermore, the simulation reveals that Syn-4 dimers act as levers, moving the cytoplasmic domains in the opposite direction of the shear flow. To quantify the cytoplasmic bending, we measured the angle θ between each cytoplasmic dimer and the z axis. Fig. 6 b shows the cosine of θ for the three cytoplasmic domains, where value 1 represents cytoplasmic alignment with the z axis and value 0 represents cytoplasmic domain is parallel to the membrane. As observed, the three cytoplasmic domains bend toward the membrane during the simulation. In endothelial cells, the Syn-4 cytoplasmic domains are connected to transduction complexes and actin filaments, and it is expected that cytoplasmic angling should move the anchoring points in the

cytoskeleton, triggering the biochemical machinery inside the cell. The [Movie S2](#) shows the flow simulation under 0.47 MPa shear stress.

Glycocalyx binding

Another puzzling aspect of the glycocalyx is its role as a flypaper for molecules flowing in the blood; that is, its ability to recognize and retain extracellular ligands. This is a critical function, because ligands deliver biochemical signals to endothelial cells. An extensive variety of HS-binding ligands has been reported, including growth factors, extracellular matrix proteins, cell-cell adhesion receptors, and blood-coagulation factors (42). Among the most studied ligands are fibroblast growth factors (FGF). The FGF family is composed of at least 20 related proteins and it is involved in several cellular functions, such as proliferation, migration, morphogenesis, and angiogenesis (61). In particular, the FGF-2 protein is a well-documented case, as several high-resolution structures of FGF-2 in contact with HS chains are available (62,63). FGF-2 functions by promoting dimerization of specific transmembrane proteins, called FGF-receptors (FGFR). FGF-2 molecules alone cannot gather FGFRs, and HS chains are needed to retain FGF-2 at the cell surface. As FGF-2s, HS chains, and FGFRs aggregate into macromolecular complexes, FGFRs dimerize and transfer the stimulus inside endothelial cells. Nevertheless, the molecular mechanism behind the aggregation of FGFs and HS chains is still a matter of debate (64).

We studied the effect of glycocalyx on FGF-2 dynamics. In principle, all-atom MD simulations can fully characterize the dynamic interplay between ligands and receptors, as it has been shown before for systems of up to 100,000 atoms (65,66). Unfortunately, the size of our glycocalyx system (5,700,000) exceeds that range. Moreover, FGF-2 is more massive than typical small ligands, and a thorough equilibration between FGF-2 and glycocalyx may require hundreds of nanoseconds or microseconds. To overcome these limitations, we employed the Grid-SMD technique, which reduces the system size by coarse-graining the atomic details of glycocalyx into a grid. Then, FGF-2 molecules diffuse on the glycocalyx grid; the interacting forces between FGF2 and glycocalyx are calculated from the grid potential. The Grid-SMD approach was initially proposed for studies of electric field-driven transport (25), and as such it is well suited to study how FGF-2 transport is affected by a highly charged polymeric brush. Grid-SMD simulations reduce the system size from millions to thousands of atoms, and smooth the energy landscape for fast FGF-2 diffusion. The grids that we employed do not take into account the steric hindrance of the glycocalyx and only consider the mean electrostatic field of the sugar chains. Recent developments in the Grid-SMD technique allow the addition of extra molecular information. For example, steric hindrance can be included by adding a sec-

ond grid potential that represents a three-dimensional potential of mean force (67,68).

For binding simulations, we performed an on-and-off MD cycle, with the glycocalyx grids acting intermittently on FGF-2 molecules under flow. The MD cycle consists of three consecutive parts: FGF-2 molecules flowing free; then flowing under the effect of glycocalyx grids; and then, finally, flowing free again. Such an MD cycle mimics the process of protein flowing, binding in the glycocalyx, and subsequent release, which can occur by enzymatic cleavage of the sugar chains (69). The [movie S3](#) shows the on-and-off MD cycle using one-dimer grid.

[Fig. 7](#) shows the effect of glycocalyx grid on FGF-2's mobility, which is characterized by measuring the FGF-2's average velocity ([Fig. 7, a and b](#)) and average position from the membrane surface ([Fig. 7, c and d](#)). [Fig. 7, a and c](#), refers to one Syn-4 dimer grid (Sim37), whereas [Fig. 7, b and d](#), refers to three Syn-4 dimer grids (Sim38).

For the first part of the cycle, the first 10 ns (Sim36; *open backgrounds at left*), the FGF-2 molecules move in the direction of the flow with varying velocities ([Fig. 7, a and b](#)), and retain their distance from the lipid surface ([Fig. 7, c and d](#)).

The second part of the cycle, the activation of glycocalyx grids, is marked by the shaded areas in [Fig. 7](#). FGF-2 molecules still move in the direction of the flow, but the grid forces slow down the proteins and the average velocities decrease ([Fig. 7, a and b](#)). Remarkably, FGF-2 molecules

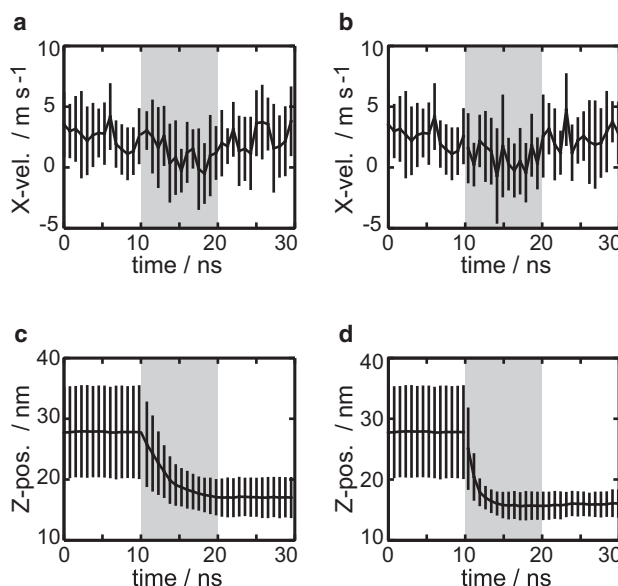


FIGURE 7 Glycocalyx affects mobility of FGF proteins. The panels show flow simulations of FGF-2s turning on and off the electrostatic potential of glycocalyx. (*Open, shaded, and open backgrounds* mark states as off, on, and off for glycocalyx electrostatic fields, respectively.) (*a and b*) Average velocities for FGFs using one-Syn-4 dimer and three-Syn dimer grids, respectively. (*c and d*) Average positions for FGFs using one-Syn-4 dimer and three-Syn dimer grids, respectively. Each point represents an average taken over 10 FGF-2s. Error bars represent \pm SD taken over 10 FGF-2s.

move close to the membrane position (Fig. 7, *c* and *d*). The FGF-2 molecules concentrate in the region of high HS charge density (time zero at Fig. 6 *a*). These simulations suggest that the glycocalyx contributes to gather FGF-2s near the lipid membrane, increasing the effective concentration of FGF-2, which is needed for FGFR activation.

The third part of the cycle is shown in open backgrounds at right. Both simulations were continued, but now the glycocalyx grids were turned off (Sim39 and 40). The FGF-2 velocities start to increase (Fig. 7, *a* and *b*); however, the position from the membrane remains unchanged (Fig. 7, *c* and *d*).

It is well established that HS induces not only binding but also oligomerization of FGFs; namely, the formation of FGF dimers or tetramers along the HS chains (70). FGF oligomerization can be an essential step for FGFR activity, as it has been hypothesized that FGF oligomers are needed for FGFR dimerization (71,72). During our binding simulations, we observed the formation of FGF-2 aggregates. Each FGF-2 protein has a charge of $+11 e$, and contains an amino-acid binding sequence KRTGQYKLGS KTGPGQK (each letter refers to one-letter abbreviation code for amino acids) to recognize HS chains. As the FGF-2 molecules race toward the negatively charged positions in the glycocalyx grids, they get close to each other and assemble into FGF-2 oligomers. To provide a quantitative description of FGF-2 oligomerization, we used an iterative nearest-neighbor search procedure to identify aggregates (73). If the centers of masses of FGF-2s are within a cutoff distance of 4 nm, the proteins are considered in contact and part of an oligomer. Fig. 8, *a* and *b*, shows the FGF-2 oligomerization for one- and three-dimer glycocalyx grids, respectively. Shaded backgrounds in the *x* axes mark the time region where the glycocalyx grids are active. Each circle represents a FGF-2 aggregate; the radius and grayscale provide information about the aggregate's size (see legend). Such snowman-like plots provide a schematic representation of the aggregation process over time.

In the first 10 ns, when the glycocalyx grids are not active, FGF-2 molecules flow individually across the periodic cell and do not oligomerize. When the grids are active (shaded backgrounds), monomers crowd near the highly charged positions in the grid (see also Fig. 7, *c* and *d*), forming oligomers of varying sizes. The most remarkable is a short-lived pentamer (snapshot in Fig. 8 *c*), which eventually breaks into a dimer and a trimer. For the last 10 ns, the grids are turned off again. The newly-formed protein-protein interfaces of dimers and trimers remain stable under the flow. The existence of similar side-by-side dimers, so-called *cis* dimers, is still under discussion (64), mostly because there is no crystallographic evidence yet. It is tempting to state that our simulations confirmed the existence of *cis* dimers. However, because the binding simulations are short, the stability of those oligomers is difficult to assess. We have inspected the trajectories of Sim37–40, where FGF2 oligomers appeared, searching for specific FGF2 contacts that

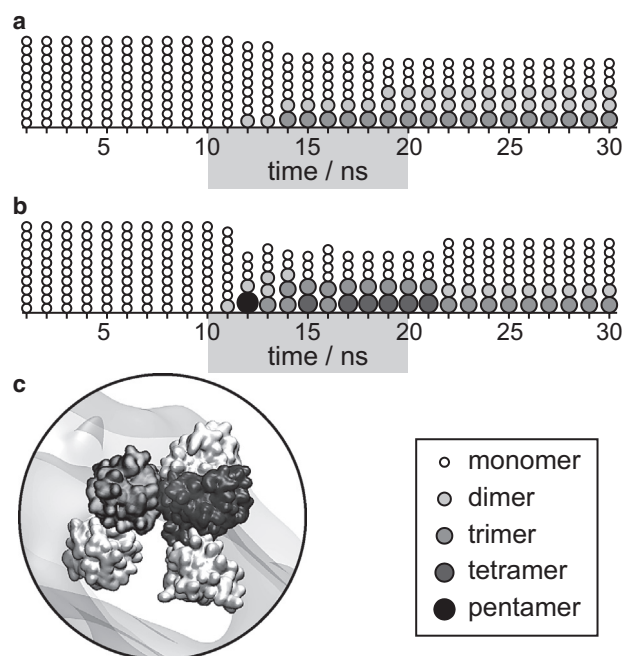


FIGURE 8 Glycocalyx induces aggregation of FGF proteins. (*a* and *b*) Flow simulations of FGFs turning on and off the electrostatic potential of glycocalyx. The images show schematic representations of FGF aggregation under the effect of one dimer (*a*) and three dimer (*b*) glycocalyx electrostatic fields. (Circles) FGF aggregates. For each time frame shown, the aggregates are sorted based on their total mass. The number of FGFs in each aggregate is coded in the size and grayscale (see inset). (Shaded backgrounds in the axes) Activation of the glycocalyx electric fields. (*c*) (Snapshot) FGF pentamer. (Transparent surface) Isosurface of electrostatic potential.

are known to stabilize in FGF2-FGFR interface (63,74). Although we were able to identify the hydrophobic patch NYL (N102-Y103-L140 in Plotnikov et al. (74)) as a part of the interface in one of the trimers, most of the contact surfaces are different. Therefore, it is likely that the oligomer contacts are nonspecific and may eventually dissociate if simulated longer.

Altogether, our results provide a generic mechanism of FGF-2-HS molecular interplay: The highly charged glycocalyx force the intrusion of FGF-2 proteins near the membrane position. Then, the negatively charged positions in the glycocalyx act as nucleation centers for FGF-2 oligomerization. FGF-2 oligomers are formed within the glycocalyx layer. Such aggregates may contribute to trigger FGFR activity. Overall, these results show the effect of the different grafting densities. The higher the concentration of HS chains, the slower the FGF-2s flow and the closer they get to the membrane. Also, the high HS concentration allow the temporal formation of large aggregates.

CONCLUSIONS

We use large-scale MD simulations to present the structure and short time dynamics of the glycocalyx layer. We have

built the most detailed to-date model of the glycocalyx, composed of HS sugar chains connected to transmembrane Syn-4 dimers embedded in a POPC lipid bilayer.

We evaluated four HS sequences containing different degrees of sulfonation, including a sequence with regions for FGF and antithrombin binding. Our results revealed that Syn-4 has α -helical segments in the ectodomain, but it is unfolded in the segments where the HS chains are linked. Furthermore, HS chains remain extended independently of the sulfonation pattern.

We examined the glycocalyx conformation under shear flow. Under moderate shear forces, we observed stretching of HS chains, thinning of the glycocalyx thickness, and bending of the Syn-4 cytoplasmic domain. This last result shows that shear stress can exert influence on intracellular structures through mechanotransduction.

We explored the binding of FGF proteins to the glycocalyx layer. We used Grid-SMD methodology to simplify the glycocalyx model, reducing the system's size from 5,700,000 to 20,000 atoms. We observed an increase of the FGF concentration near negative charges on the HS chains, leading to FGF oligomerization.

Overall, our results provide insights in the structure of glycocalyx layer and its dynamics, albeit for nanosecond timescales. Our findings motivate the need for further improvements; for example, adding different proteoglycans and sugar chains, including more atomic complexity into the glycocalyx grids, and suitable coarse-graining of the glycocalyx network to reach longer timescales. We envision that simulations of flow in capillaries that accurately include the effects of the glycocalyx will lead to a more comprehensive understanding of blood flow in health and disease.

SUPPORTING MATERIAL

Directions on obtaining glycocalyx structures and Grid-SMD simulations, two figures, one table, and three movies are available at [http://www.biophysj.org/biophysj/supplemental/S0006-3495\(13\)01201-0](http://www.biophysj.org/biophysj/supplemental/S0006-3495(13)01201-0).

We thank C. Mei from the Parallel Programming Laboratory at the University of Illinois at Urbana-Champaign for extending the NAMD software to allow compression of branched polymers.

We acknowledge supercomputer time provided by the Swiss Supercomputer Centre (CSCS) and by the Brutus Cluster at ETH (Eidgenössische Technische Hochschule) Zürich. This work was supported by the Swiss National Science Foundation (grant No. 138231).

REFERENCES

- Pries, A. R., T. W. Secomb, and P. Gaehtgens. 2000. The endothelial surface layer. *Pflugers Arch.* 440:653–666.
- Aird, W. C. 2007. Phenotypic heterogeneity of the endothelium: II. Representative vascular beds. *Circ. Res.* 100:174–190.
- Aird, W. C. 2007. Phenotypic heterogeneity of the endothelium: I. Structure, function, and mechanisms. *Circ. Res.* 100:158–173.
- Aird, W. C. 2008. Endothelium in health and disease. *Pharmacol. Rep.* 60:139–143.
- Kang, D. H., J. Kanellis, ..., R. J. Johnson. 2002. Role of the microvascular endothelium in progressive renal disease. *J. Am. Soc. Nephrol.* 13:806–816.
- Reitsma, S., D. W. Slaaf, ..., M. G. oude Egbrink. 2007. The endothelial glycocalyx: composition, functions, and visualization. *Pflugers Arch.* 454:345–359.
- Luft, J. H. 1966. Fine structures of capillary and endocapillary layer as revealed by Ruthenium Red. *Fed. Proc.* 25:1773–1783.
- Nieuwdorp, M., M. C. Meuwese, ..., E. S. G. Stroes. 2005. The endothelial glycocalyx: a potential barrier between health and vascular disease. *Curr. Opin. Lipidol.* 16:507–511.
- Nieuwdorp, M., H. L. Mooij, ..., H. Vink. 2006. Endothelial glycocalyx damage coincides with microalbuminuria in type 1 diabetes. *Diabetes.* 55:1127–1132.
- Espinosa-Marzal, R. M., G. Fontani, ..., R. Crockett. 2013. Sugars communicate through water: oriented glycans induce water structuring. *Biophys. J.* 104:2686–2694.
- Sugihara-Seki, M., T. Akinaga, and T. Itano. 2008. Flow across microvessel walls through the endothelial surface glycocalyx and the interendothelial cleft. *J. Fluid Mech.* 601:229–252.
- Fu, B. M., B. Chen, and W. Chen. 2003. An electrodiffusion model for effects of surface glycocalyx layer on microvessel permeability. *Am. J. Physiol. Heart C.* 284:H1240–H1250.
- Agrawal, N. J., and R. Radhakrishnan. 2007. The role of glycocalyx in nanocarrier-cell adhesion investigated using a thermodynamic model and Monte Carlo simulations. *J. Phys. Chem. C Nanomater. Interfaces.* 111:15848–15856.
- Binder, K., T. Kreer, and A. Milchev. 2011. Polymer brushes under flow and in other out-of-equilibrium conditions. *Soft Matter.* 7:7159–7172.
- Weinbaum, S., X. Zhang, ..., S. C. Cowin. 2003. Mechanotransduction and flow across the endothelial glycocalyx. *Proc. Natl. Acad. Sci. USA.* 100:7988–7995.
- Eriksson, M., T. K. Lindhorst, and B. Hartke. 2008. Differential effects of oligosaccharides on the hydration of simple cations. *J. Chem. Phys.* 128:105105–105110.
- Lee, E. H., J. Hsin, ..., K. Schulten. 2009. Discovery through the computational microscope. *Structure.* 17:1295–1306.
- Khalili-Araghi, F., J. Gumbart, ..., K. Schulten. 2009. Molecular dynamics simulations of membrane channels and transporters. *Curr. Opin. Struct. Biol.* 19:128–137.
- Schreiner, E., L. G. Trabuco, ..., K. Schulten. 2011. Stereochemical errors and their implications for molecular dynamics simulations. *BMC Bioinform.* 12:190.
- MacKenzie, K. R., J. H. Prestegard, and D. M. Engelman. 1997. A transmembrane helix dimer: structure and implications. *Science.* 276:131–133.
- Humphrey, W., A. Dalke, and K. Schulten. 1996. VMD: visual molecular dynamics. *J. Mol. Graph.* 14:33–38, 27–28.
- Shin, J., W. Lee, ..., E. S. Oh. 2001. Solution structure of the dimeric cytoplasmic domain of syndecan-4. *Biochemistry.* 40:8471–8478.
- Aksimentiev, A., R. K. Brunner, ..., K. Schulten. 2009. Modeling transport through synthetic nanopores. *IEEE Nanotechnol.* 3:20–28.
- Trabuco, L. G., E. Villa, ..., K. Schulten. 2008. Flexible fitting of atomic structures into electron microscopy maps using molecular dynamics. *Structure.* 16:673–683.
- Wells, D. B., V. Abramkina, and A. Aksimentiev. 2007. Exploring transmembrane transport through α -hemolysin with grid-steered molecular dynamics. *J. Chem. Phys.* 127:125101.
- Aksimentiev, A., and K. Schulten. 2005. Imaging α -hemolysin with molecular dynamics: ionic conductance, osmotic permeability, and the electrostatic potential map. *Biophys. J.* 88:3745–3761.

27. Phillips, J. C., R. Braun, ..., K. Schulten. 2005. Scalable molecular dynamics with NAMD. *J. Comput. Chem.* 26:1781–1802.
28. MacKerell, Jr., A. D., D. Bashford, ..., M. Karplus. 1998. All-atom empirical potential for molecular modeling and dynamics studies of proteins. *J. Phys. Chem. B.* 102:3586–3616.
29. Jorgensen, W. L., J. Chandrasekhar, ..., M. L. Klein. 1983. Comparison of simple potential functions for simulating liquid water. *J. Chem. Phys.* 79:926–935.
30. Guvench, O., S. S. Mallajosyula, ..., A. D. MacKerell, Jr. 2011. CHARMM additive all-atom force field for carbohydrate derivatives and its utility in polysaccharide and carbohydrate-protein modeling. *J. Chem. Theory Comput.* 7:3162–3180.
31. Mallajosyula, S. S., O. Guvench, ..., A. D. MacKerell, Jr. 2012. CHARMM additive all-atom force field for phosphate and sulfate linked to carbohydrates. *J. Chem. Theory Comput.* 8:759–776.
32. Hatcher, E. R., O. Guvench, and A. D. MacKerell, Jr. 2009. CHARMM additive all-atom force field for acyclic polyalcohols, acyclic carbohydrates and inositol. *J. Chem. Theory Comput.* 5:1315–1327.
33. Huige, C. J. M., and C. Altona. 1995. Force field parameters for sulfates and sulfamates based on ab initio calculations: extensions of AMBER and CHARMM fields. *J. Comput. Chem.* 16:56–79.
34. Tanner, D. E., K. Y. Chan, ..., K. Schulten. 2011. Parallel generalized Born implicit solvent calculations with NAMD. *J. Chem. Theory Comput.* 7:3635–3642.
35. Mei, C., Y. Sun, ..., C. Harrison. 2011. Enabling and scaling biomolecular simulations of 100 million atoms on petascale machines with a multicore-optimized message-driven runtime. In *Proceedings of the 2011 ACM/IEEE Conference on Supercomputing*, Seattle, WA. Institute of Electrical and Electronics Engineers (IEEE), New York. 1–11.
36. González, M. A., and J. L. F. Abascal. 2010. The shear viscosity of rigid water models. *J. Chem. Phys.* 132:096101–096102.
37. Kronn-Batenburg, L. M. J., P. H. Kruiskamp, ..., J. Kroon. 1997. Estimation of the persistence length of polymers by MD simulations on small fragments in solution. Application to cellulose. *J. Phys. Chem. B.* 101:8454–8459.
38. Squire, J. M., M. Chew, ..., C. Michel. 2001. Quasi-periodic substructure in the microvessel endothelial glycocalyx: a possible explanation for molecular filtering? *J. Struct. Biol.* 136:239–255.
39. Megens, R. T. A., S. Reitsma, ..., M. A. van Zandvoort. 2007. Two-photon microscopy of vital murine elastic and muscular arteries. Combined structural and functional imaging with subcellular resolution. *J. Vasc. Res.* 44:87–98.
40. van den Berg, B. M., H. Vink, and J. A. E. Spaan. 2003. The endothelial glycocalyx protects against myocardial edema. *Circ. Res.* 92:592–594.
41. Couchman, J. R. 2010. Transmembrane signaling proteoglycans. *Annu. Rev. Cell Dev. Biol.* 26:89–114.
42. Carey, D. J. 1997. Syndecans: multifunctional cell-surface co-receptors. *Biochem. J.* 327:1–16.
43. Weinbaum, S., J. M. Tarbell, and E. R. Damiano. 2007. The structure and function of the endothelial glycocalyx layer. *Annu. Rev. Biomed. Eng.* 9:121–167.
44. Bishop, J. R., M. Schuksz, and J. D. Esko. 2007. Heparan sulphate proteoglycans fine-tune mammalian physiology. *Nature.* 446:1030–1037.
45. Esko, J. D., and S. B. Selleck. 2002. Order out of chaos: assembly of ligand binding sites in heparan sulfate. *Annu. Rev. Biochem.* 71:435–471.
46. Ly, M., F. E. Leach, 3rd, ..., R. J. Linhardt. 2011. The proteoglycan bikunin has a defined sequence. *Nat. Chem. Biol.* 7:827–833.
47. Schenauer, M. R., J. K. Meissen, ..., J. A. Leary. 2009. Heparan sulfate separation, sequencing, and isomeric differentiation: ion mobility spectrometry reveals specific iduronic and glucuronic acid-containing hexasaccharides. *Anal. Chem.* 81:10179–10185.
48. Wu, Z. L., and M. Lech. 2005. Characterizing the non-reducing end structure of heparan sulfate. *J. Biol. Chem.* 280:33749–33755.
49. Perrimon, N., and M. Bernfield. 2000. Specificities of heparan sulphate proteoglycans in developmental processes. *Nature.* 404:725–728.
50. Bernfield, M., M. Götte, ..., M. Zako. 1999. Functions of cell surface heparan sulfate proteoglycans. *Annu. Rev. Biochem.* 68:729–777.
51. Freddolino, P. L., C. B. Harrison, ..., K. Schulten. 2010. Challenges in protein folding simulations: timescale, representation, and analysis. *Nat. Phys.* 6:751–758.
52. Deng, M., X. Li, ..., G. E. Karniadakis. 2012. Simulation and modeling of slip flow over surfaces grafted with polymer brushes and glycocalyx fibers. *J. Fluid Mech.* 711:192–211.
53. Bass, M. D., and M. J. Humphries. 2002. Cytoplasmic interactions of syndecan-4 orchestrate adhesion receptor and growth factor receptor signaling. *Biochem. J.* 368:1–15.
54. Dews, I. C., and K. R. MacKenzie. 2007. Transmembrane domains of the syndecan family of growth factor coreceptors display a hierarchy of homotypic and heterotypic interactions. *Proc. Natl. Acad. Sci. USA.* 104:20782–20787.
55. Psachoulia, E., D. P. Marshall, and M. S. P. Sansom. 2010. Molecular dynamics simulations of the dimerization of transmembrane α -helices. *Acc. Chem. Res.* 43:388–396.
56. Waters, S. L., J. Alastruey, ..., F. N. van de Vosse. 2011. Theoretical models for coronary vascular biomechanics: progress and challenges. *Prog. Biophys. Mol. Biol.* 104:49–76.
57. Hecker, M., A. Mülsch, ..., R. Busse. 1993. Vasoconstriction and increased flow: two principal mechanisms of shear stress-dependent endothelial autacoid release. *Am. J. Physiol. Heart C.* 265:H828–H833.
58. Vink, H., and B. R. Duling. 2000. Capillary endothelial surface layer selectively reduces plasma solute distribution volume. *Am. J. Physiol. Heart C.* 278:H285–H289.
59. Florian, J. A., J. R. Kosky, ..., J. M. Tarbell. 2003. Heparan sulfate proteoglycan is a mechanosensor on endothelial cells. *Circ. Res.* 93:e136–e142.
60. Gouverneur, M., J. A. E. Spaan, ..., H. Vink. 2006. Fluid shear stress stimulates incorporation of hyaluronan into endothelial cell glycocalyx. *Am. J. Physiol. Heart C.* 290:H458–H462.
61. Faham, S., R. J. Linhardt, and D. C. Rees. 1998. Diversity does make a difference: fibroblast growth factor-heparin interactions. *Curr. Opin. Struct. Biol.* 8:578–586.
62. Faham, S., R. E. Hileman, ..., D. C. Rees. 1996. Heparin structure and interactions with basic fibroblast growth factor. *Science.* 271:1116–1120.
63. Schlessinger, J., A. N. Plotnikov, ..., M. Mohammadi. 2000. Crystal structure of a ternary FGF-FGFR-heparin complex reveals a dual role for heparin in FGFR binding and dimerization. *Mol. Cell.* 6:743–750.
64. Waksman, G., and A. B. Herr. 1998. New insights into heparin-induced FGF oligomerization. *Nat. Struct. Biol.* 5:527–530.
65. Isgro, T. A., and K. Schulten. 2005. Binding dynamics of isolated nucleoporin repeat regions to importin- β . *Structure.* 13:1869–1879.
66. Isgro, T. A., and K. Schulten. 2007. Association of nuclear pore FG-repeat domains to NTF2 import and export complexes. *J. Mol. Biol.* 366:330–345.
67. Carr, R., J. Comer, ..., A. Aksimentiev. 2011. Atoms-to-microns model for small solute transport through sticky nanochannels. *Lab Chip.* 11:3766–3773.
68. Comer, J., and A. Aksimentiev. 2012. Predicting the DNA sequence dependence of nanopore ion current using atomic-resolution Brownian dynamics. *J. Phys. Chem. C.* 116:3376–3393.
69. Vlodavsky, I., O. Goldshmidt, ..., Y. Friedmann. 2002. Mammalian heparanase: involvement in cancer metastasis, angiogenesis and normal development. *Semin. Cancer Biol.* 12:121–129.

70. Venkataraman, G., Z. Shriver, ..., R. Sasisekharan. 1999. Fibroblast growth factors 1 and 2 are distinct in oligomerization in the presence of heparin-like glycosaminoglycans. *Proc. Natl. Acad. Sci. USA*. 96:1892–1897.
71. Spivak-Kroizman, T., M. A. Lemmon, ..., I. Lax. 1994. Heparin-induced oligomerization of FGF molecules is responsible for FGF receptor dimerization, activation, and cell proliferation. *Cell*. 79:1015–1024.
72. Herr, A. B., D. M. Ornitz, ..., G. Waksman. 1997. Heparin-induced self-association of fibroblast growth factor-2. Evidence for two oligomerization processes. *J. Biol. Chem.* 272:16382–16389.
73. Cruz-Chu, E. R., and K. Schulten. 2010. Computational microscopy of the role of protonable surface residues in nanoprecipitation oscillations. *ACS Nano*. 4:4463–4474.
74. Plotnikov, A. N., J. Schlessinger, ..., M. Mohammadi. 1999. Structural basis for FGF receptor dimerization and activation. *Cell*. 98:641–650.